

Check for updates

A Neuromorphic Multifunctional Sensing Fiber for Deep Learning Enhanced Wearable Human-Machine Interaction

Xin Chen, Jiechun Zhou, Jinrong Huang, * Jiahui Liu, Lanyu Nie, and Yutian Zhu*

Next-generation human-machine interaction demands neuromorphic input pathways that can seamlessly encode human intent with spatial precision, flexibility, and artificial intelligence (AI) compatibility. Conventional tactile systems often rely on multi-electrode matrices for localization, resulting in complex wiring, crosstalk, and limited textile integration. Here, a neuromorphic multifunctional sensing single-fiber (MSSF) fabricated via melt-extrusion 3D printing of a thermoplastic polyurethane/ionic liquid ionogel is presented that can achieve continuous touch position decoding with only terminal electrodes. A folded-parallel configuration modulates the distributed electric field along the fiber, allowing contact-induced capacitance variations to be mathematically mapped to location with millimeter-level resolution. Moreover, MSSF additionally enables high-sensitivity strain and temperature sensing. Coupled with deep neural networks, the system achieves 100% recognition accuracy in touch intent and gestures. MSSF forms an integrated perception-transmission-recognition-feedback loop within a scalable, textile-compatible architecture, offering a transformative platform for embodied, intelligent, and spatially aware human-machine interfaces.

1. Introduction

With the rapid development of virtual reality (VR) and augmented reality (AR) technologies, immersive human-machine interaction (HMI) systems are gradually extending to key application domains such as education, healthcare, gaming, and remote collaboration.^[1,2] The key to achieving high immersion and natural interactive experience lies in establishing a "body-as-interface" interaction paradigm, enabling systems to perceive user movements, tactile input, and physiological states in real time, and to generate intelligent feedback accordingly.^[3–6] To achieve this goal, sensing systems are evolving from traditional functional stacking toward neuromorphic architectures with integrated capabilities of perception, transmission, recognition,

X. Chen, J. Zhou, J. Huang, J. Liu, L. Nie, Y. Zhu College of Material, Chemistry and Chemical Engineering Key Laboratory of Organosilicon Chemistry and Material Technology Ministry of Education

Key Laboratory of Organosilicon Material Technology Hangzhou Normal University

Hangzhou, Zhejiang 311121, China

E-mail: jinronghuang@hznu.edu.cn; ytzhu@hznu.edu.cn

The ORCID identification number(s) for the author(s) of this article can be found under https://doi.org/10.1002/adfm.202524652

DOI: 10.1002/adfm.202524652

and feedback, thereby closing the signal loop within flexible and wearable platforms. $^{[7-10]}$

Among various perception tasks, tactile sensing serves as the most fundamental and direct channel for HMI.[11-13] Its spatial resolution, response speed, and integration flexibility critically dominate the naturalness and immersiveness of the interaction.[14] Most existing tactile localization strategies still rely on 2D electrode arrays or resistive/capacitive matrices, inferring contact positions based on signal differences among nodes.[15,16] These architectures require many sensing elements and interconnects, introducing complex wiring, encapsulation, and signal readout circuits, and often lead to issues such as crosstalk and mechanical incompatibility, severely limiting the practicality and scalability of flexible wearable systems. Especially for the construction of conformal, lowpower, and multifunctional sensory networks, how to reduce structural complexity, improve spatial resolution, and generate

structured outputs directly decodable by AI models remains a critical challenge.

To address the above issues, recent advances in flexible electronics have enabled the emergence of fiber-based architectures as ideal building blocks for wearable distributed sensing networks, owing to their inherent softness, stretchability, and compatibility with textile fabrication.[17,18] Compared to film-based or patch-based sensors, fiber devices can be imperceptibly integrated into key garment regions, offering multi-channel layout potential and high wearing comfort.[19-21] Existing studies have demonstrated single-modal perception capabilities such as strain or temperature sensing through material blending, interfacial engineering, and microstructural optimization.[22,23] For example, Ahmed et al. developed smart textiles integrating piezoelectric transducers and acoustic waveguide fibers, achieving multifunctional performance in health monitoring and tactile recognition, and showcasing the application potential of flexible fiber structures in diverse scenarios.[24]

Nevertheless, such multi-unit and multi-node configurations still require multiple discrete units for multifunctional sensing integration, making it difficult to achieve simplified structures and unified signal representation. Against this backdrop, single-fiber sensors, due to their 1D linear morphology, not only significantly reduce structural complexity but also offer inherent

16163028, 0, Downloaded from https://advanced.onlinelibrary.wiley.com/doi/10.1002/adfm.202524652 by Hangzhou Normal University, Wiley Online Library on [10/11/2025]. See the Terms and Conditions (https://onlinelibrary.wiley

ind-conditions) on Wiley Online Library for rules of use; OA articles are governed by the applicable Creative Commons License

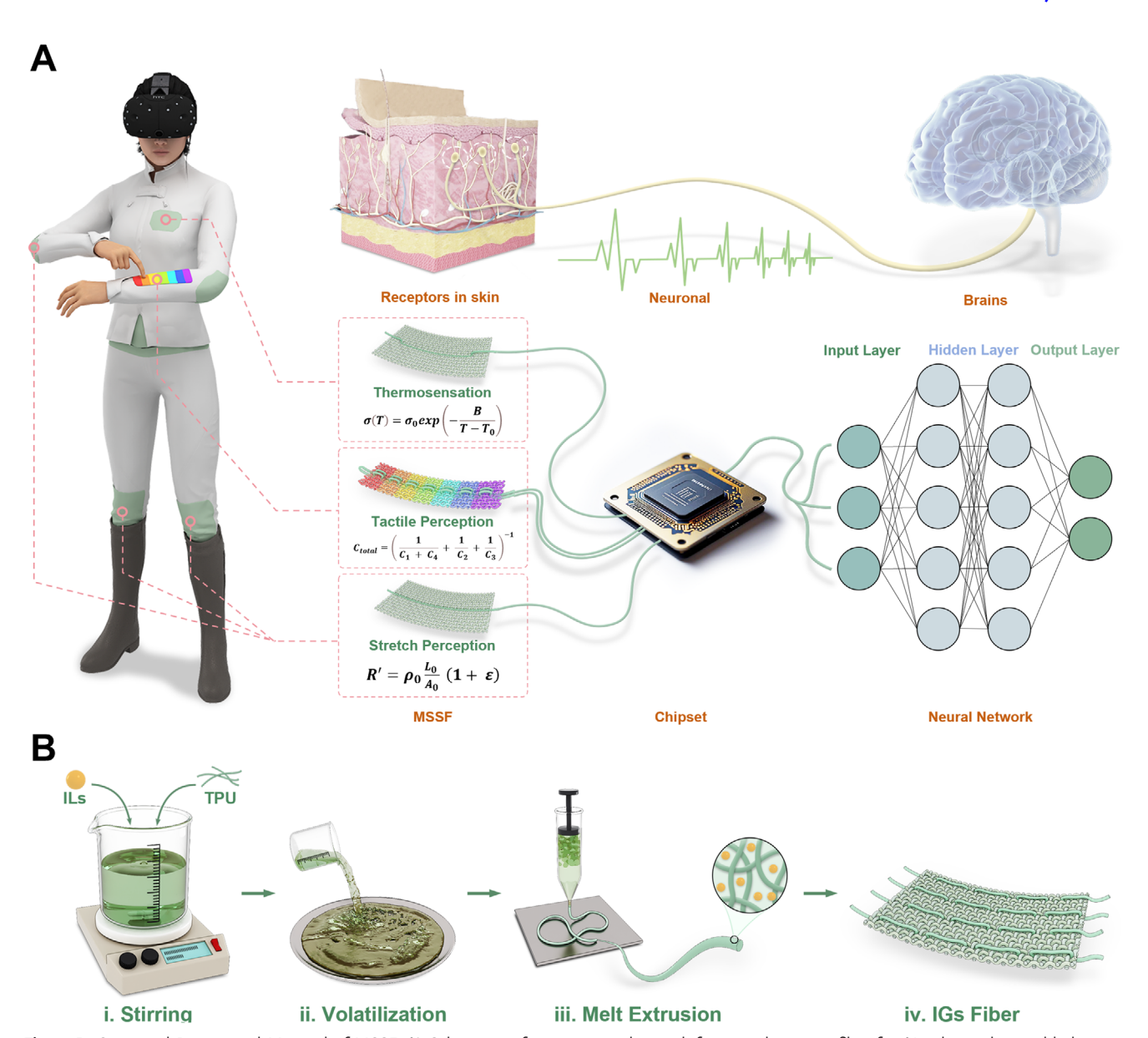


Figure 1. Structural Design and Material of MSSF. A) Schematic of a neuromorphic multifunctional sensing fiber for Al-enhanced wearable human-machine interaction. B) Structural Design and Material of MSSF.

potential for simultaneous signal sensing and transmission, making them ideal core units for constructing neuromorphic input pathways.^[25–27] Several studies have demonstrated their feasibility in single-modality domains such as strain or temperature.^[28] However, it remains a key challenge to build a single-fiber that can sense multiple physical signals with high sensitivity, ensure stable transmission, and produce structured outputs compatible with neural networks.

Here, we present a neuromorphic multifunctional sensing single-fiber (MSSF) that integrates tactile, strain, and temperature sensing within a structurally simple, textile-compatible, and AI-native architecture (**Figure 1A**). Constructed from a thermoplastic polyurethane/ionic liquid composite and fabricated via melt-extrusion 3D printing technique, MSSF achieves scalable production with high structural uniformity. Critically, MSSF in-

troduces an original folded-parallel configuration that enables tactile position localization along a single-fiber using only terminal electrodes, without requiring any spatially distributed electrode arrays. This compact design achieves millimeter-level resolution and fast response (<16 ms). Combined with convolutional neural networks (CNNs) for time-series feature extraction and classification, MSSF enables precise decoding of tactile trajectories and user intent. Beyond tactile input, MSSF also supports strain sensing across a 0–900% tensile range (gauge factor (GF) = 2.1, detection limit = 0.1%) as well as temperature sensing from 30 to 100 °C with high sensitivity (4.04% °C $^{-1}$) and fine resolution (0.1 °C), enabling comprehensive perception of biomechanical and thermal signals. This work demonstrates a unified neuromorphic sensing architecture that seamlessly integrates perception, transmission, recognition, and feedback into

www.afm-journal.de

1616928, 0, Downloaded from https://advanced.onlinelibrary.wiley.com/doi/10.1002adfm.20254655 by Hangzhou Normal University, Wiley Online Library on [10.11.12025]. See the Terms and Conditions (https://onlinelibrary.wiley.com/terms-and-conditions) on Wiley Online Library for rules of use; OA articles are governed by the applicable Ceravive Commons

a single-fiber, providing a scalable and intelligent foundation for next-generation wearable HMI.

2. Results

2.1. Structural Design and Material of MSSF

One of the core challenges in developing neuromorphic, multifunctional wearable HMI systems lies in achieving a balance between mechanical flexibility, signal sensitivity, and structural integration at the fiber scale. Accordingly, constructing a multifunctional sensing single-fiber with high structural uniformity, excellent electrical responsiveness, and textile compatibility is essential for advancing such systems toward practical and engineering deployment. To address these requirements, the design of MSSF focuses on the coordinated optimization of material composition and structural configuration, providing a robust foundation for integrated sensory platforms.

In terms of material composition, as shown in Figure 1B(i,ii), MSSF is constructed via a melt-blending strategy combining thermoplastic polyurethane (TPU) with ionic liquid (IL). The IL offers high ionic mobility and strong polarizability, endowing the sensing fiber with excellent dielectric responsiveness and temperature sensitivity. Meanwhile, TPU exhibits good processability with a 3D crosslinked network, which can facilitate the formation of stable ion transport pathways inside, thereby ensuring long-term signal stability under dynamic wearable conditions.

In terms of structural fabrication, as shown in Figure 1B(iii) and Figure S1 (Supporting Information), melt-extrusion-based 3D printing was employed to precisely construct the fiber morphology, enabling continuous formation and diameter-tunable, scalable production of MSSF. This process significantly improves the reproducibility and structural uniformity of fabrication, while also supporting customization for specific application scenarios. For example, fibers with larger diameters exhibit greater mechanical strength and strain-buffering capability, making them suitable for strain monitoring in highly dynamic regions such as joints. In contrast, smaller-diameter fibers offer enhanced flexibility and weavability, allowing for imperceptible integration into garment surfaces for high-resolution tactile sensing. To further assess batch-to-batch consistency, five MSSF samples were fabricated using identical material ratios and processing parameters. As summarized in Table S1 (Supporting Information), the measured diameters, capacitances, and resistances of these samples show minimal variation, confirming the excellent reproducibility and stability of our fabrication approach.

Figure S2A (Supporting Information) presents the scanning electron microscopy (SEM) images of MSSF samples with different diameters (1.0, 0.8, 0.6, and 0.4 mm, respectively). The results demonstrate that the fibers possess uniform surface morphology, well-defined contours, and precisely controlled dimensions, validating the stability and controllability of the melt-extrusion process for structural regulation. To further investigate the internal homogeneity and interfacial distribution of the composite, as shown in Figure S2B (Supporting Information), SEM and energy-dispersive spectroscopy (EDS) analyses were conducted on the cross-sections and lateral surfaces of the fibers. The elemental mapping reveals that fluorine (F) and sulfur (S), characteristic elements of IL, are uniformly distributed throughout

the TPU matrix, indicating good dispersion of IL within the TPU matrix.

Such a highly homogeneous composite structure facilitates the formation of stable ionic pathways, enhances overall dielectric performance, and significantly improves the mechanical robustness of the fiber, thereby mitigating structural fatigue and signal drift commonly observed in flexible sensors under dynamic conditions. As shown in Figure 1B(iv), the MSSF achieves a balanced combination of stretchability and wearability, effectively addressing the long-standing trade-off between mechanical and electrical performance in flexible sensors, and providing a solid functional foundation for multifunctional wearable HMI.

2.2. Touch Perception Mechanism of MSSF

To achieve high-precision touch perception, we designed an innovative structure based on a capacitive mechanism and conducted both theoretical modeling and experimental validation to investigate its working principle. Initial measurements of the intrinsic capacitance of the TPU@IL ionogel-based single-fiber revealed a clear negative correlation between capacitance and fiber length (Figure S3, Supporting Information). This trend is consistent with the classical capacitance model for a dielectric cylinder, expressed as:

$$C = \varepsilon_{\gamma} \cdot \varepsilon_0 \cdot \frac{A}{I} \tag{1}$$

Here, C denotes the capacitance of a single-fiber, ε_{γ} is the relative permittivity of the material, ε_{n} is the vacuum permittivity, A is the cross-sectional area of the fiber, and L is the fiber length. This relationship indicates that, with fixed fiber geometry and material parameters, the capacitance decreases as the length L increases. This theoretical correlation not only reveals the fundamental influence of fiber configuration on sensing sensitivity but also provides a theoretical basis for the subsequent development of the touch sensing system.

Based on the aforementioned capacitance-length relationship, we established the touch sensing structure and equivalent model of MSSF. As illustrated in Figure 2A(i), the proposed sensing mechanism adopts a folded-parallel configuration using a single ionogel fiber: the fiber is folded at its midpoint to form a symmetric structure, with electrodes connected to both ends. In the absence of contact, the corresponding capacitance is denoted as C_0 . When a finger touches any point along the fiber, the contact point divides the fiber into three segments: the right segment is denoted as C_1 and the left segment is further divided into C_2 and C_3 . Simultaneously, the finger introduces an additional human body capacitance C_4 . Under this condition, the total capacitance measured across the electrodes can be expressed as a composite network in which C_1 is in parallel with C_4 , and the resulting parallel branch is in series with C_2 and C_3 . The total capacitance C_{total} is given by:

$$C_{total} = \left(\frac{1}{C_1 + C_4} + \frac{1}{C_2} + \frac{1}{C_3}\right)^{-1} \tag{2}$$

Since the human body capacitance C_4 is relatively constant and significantly larger than C_1 , and C_2 and C_3 are equal in length and

16163028, 0, Downloaded from https://advanced.onlinelibrary.wiley.com/doi/10.1002/adfm.202524652 by Hangzhou Normal University, Wiley Online Library on [10/11/2025]. See the Terms

and-conditions) on Wiley Online Library for rules of use; OA articles are governed by the applicable Creative Commons License

www.afm-journal.de

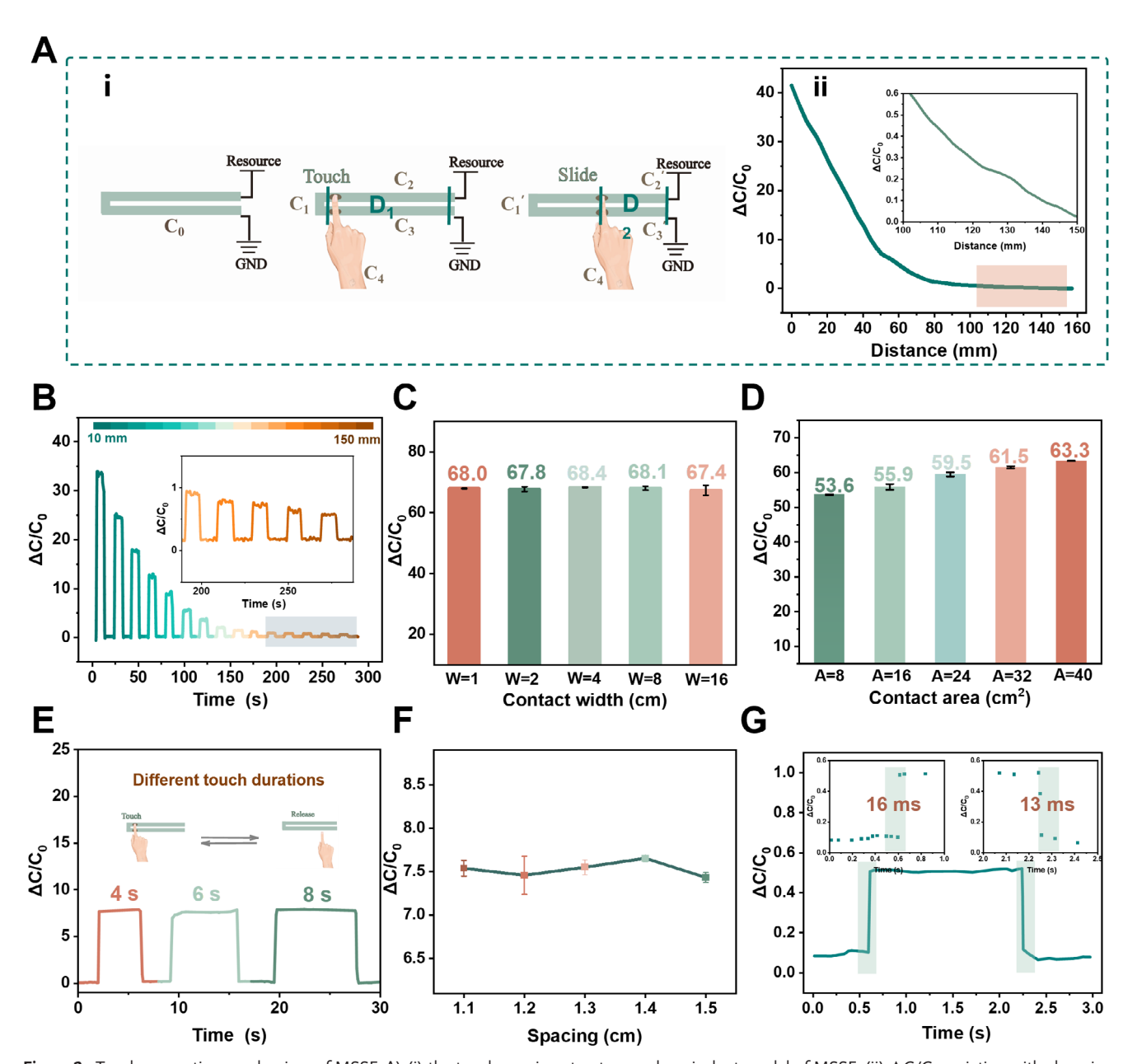


Figure 2. Touch perception mechanism of MSSF. A) (i) the touch sensing structure and equivalent model of MSSF, (ii) $\Delta C/C_0$ variation with changing touch position relative to the electrode under continuous sliding. B) $\Delta C/C_0$ variation with changing touch position relative to the electrode under intermittent pressing. C) Effect of contact width on $\Delta C/C_0$. D) Effect of contact area on $\Delta C/C_0$. E) Effect of pressing duration on capacitive signals. F) Influence of inter-fiber spacing on output capacitance. G) Measurement of the touch response/recovery time of the sensor.

thus approximately equal in value, Equation (2) can be simplified by substituting Equation (1) as follows:

$$C_{total} \approx \frac{1}{\frac{1}{C_4} + \frac{2D}{\varepsilon_{\nu}\varepsilon_0 A}} \tag{3}$$

Let $B=1/C_{4,}$ $K=2/(\varepsilon_{\gamma}\varepsilon_{0}A)$, then Equation (3) can be further simplified as:

$$C_{total} \approx \frac{1}{B + KD}$$
 (4)

Here, D represents the distance between the touch point and the electrode end. Based on the above model, a mathematical mapping was established between the sensor's capacitance C_{total} and the touch position D, providing theoretical support for subsequent touch localization and behavior interpretation. Figure 2A(ii) and Video S1 (Supporting Information) present the experimental validation, where the normalized capacitance change ($\Delta C/C_0$) exhibits a monotonic increase as the finger slides along the fiber toward the electrode. That is, the closer the contact point is to the electrode, the stronger the capacitive response. The experimental results show excellent agreement with

www.afm-journal.de

1616328, D. Downloaded from https://advanced.onlinelibrary.wiley.com/doi/10.1002/adfm.20324652 by Hangzhou Normal University, Wiley Online Library on [10/11/2025]. See the Terms and Conditions (https://onlinelibrary.wiejc.com/terms-and-conditions) on Wiley Online Library for rules of use; OA articles are governed by the applicable Creative Commons License

theoretical predictions, confirming the accuracy and feasibility of the proposed physical model. Furthermore, Figure 2B and Video S2 (Supporting Information) display the capacitive response characteristics under intermittent pressing at different touch positions. Repeated tests demonstrate that the sensor yields highly consistent output for the same location, with minimal signal fluctuation, indicating excellent spatial resolution and response repeatability. These results provide a reliable basis for high-precision touch localization perception and real-time gesture tracking.

In addition, touch response measurements across different fiber diameters (1.0, 0.8, and 0.6 mm, respectively) revealed a clear positive correlation in capacitance values at the same contact position (10 mm). According to the equation $K=2/(\epsilon_{\gamma}\epsilon_{0}A)$, a larger cross-sectional area (A) results in a smaller K, thereby increasing the C_{total} . As shown in Figure S4A,B (Supporting Information), the ΔC values of the fiber with a diameter of 1.0 mm are significantly higher than those of the smaller-diameter fibers at the same touch position, further validating the theoretical model and providing guidance for optimal dimensional design in system configuration.

To further evaluate the geometric adaptability of MSSF to complex touch patterns, we systematically tested its capacitive response under conditions where the contact area remained constant while the aspect ratio varied (Figure 2C). A series of contactors with identical contact area (16 cm²) but varying lateral widths (from 1 to 16 cm) were used to simulate different finger or palm sizes. The results show that, under constant contact area, the variation in contactor width has a negligible effect on sensor output, with capacitance fluctuations remaining within ± 0.5 pF. This indicates that MSSF exhibits strong robustness to contact geometry and is insensitive to changes in aspect ratio. Furthermore, Figure 2D shows the capacitance response of MSSF to varying contact areas ranging from 8 to 40 cm2. As the contact area increases, the output capacitance displays a stable linear increase, demonstrating excellent area-responsiveness. This characteristic suggests that, in addition to touch position recognition, the sensor also possesses the capability for contact area discrimination, enabling richer interpretations of interactive behavior, thereby providing an additional sensory channel for multi-dimensional interaction.

In addition, the sensor's adaptability for operation rhythm and structural tolerance was investigated. Figure 2E,F present the capacitance response of MSSF under different pressing durations (2-8 s) and varying fiber-to-fiber distances (1.1-1.5 cm), respectively. The results indicate that the sensor output remains stable regardless of pressing duration or structural spacing, demonstrating excellent tolerance to temporal variation and structural deviation. These observations suggest that MSSF is well-suited for real-world wearable applications involving irregular operational rhythms and non-ideal mechanical configurations. In terms of dynamic performance, Figure 2G shows that MSSF exhibits fast tactile response, with response and recovery times of 16 and 13 ms, respectively, fully meeting the millisecond-level feedback requirements of VR systems. The rapid response not only ensures that user actions can be captured in real time but also effectively reduces interaction errors caused by latency. Regarding long-term reliability, Figure \$5 (Supporting Information) presents the sensor's performance over 5000 consecutive touchrelease cycles. The results indicate that under prolonged high-frequency operation, the capacitance signal remains stable without noticeable drift or degradation, verifying the excellent electrical stability and mechanical durability of MSSF.

Furthermore, we systematically examined the influence of ambient temperature on tactile localization accuracy (Figure S6, Supporting Information). The results show that the initial capacitance (C_0) increases gradually as temperature rises under ambient conditions, with a pronounced jump observed beyond 40 °C. Measurements of $\Delta C/C_0$ vs touch position at 25, 40, and 60 °C confirm that localization performance can be preserved through pre-calibration. Specifically, a database of calibration curves under different temperatures can be established, the ambient temperature can then be determined in real time by measuring C_0 , and the corresponding calibration curve can be applied to compute the touch position. This strategy ensures robust tactile sensing accuracy even under varying thermal environments, which is essential for reliable operation in practical wearable and outdoor scenarios.

This characteristic is of great importance for sustained, high-density HMI in VR/AR systems and ensures the long-term operational reliability of the sensor in practical wearable applications.

The touch perception mechanism of MSSF not only features a well-defined and analytically tractable physical model, but also demonstrates high spatial sensitivity, fast response, excellent stability, and strong robustness. It establishes a quantifiable and derivable mapping between touch behavior and perceptual signals, serving as a fundamental sensory basis for realizing touch intention recognition.

2.3. Wearable Tactile Interaction System

To validate the applicability and functionality of the developed MSSF in real-world HMI scenarios, we designed and implemented two representative interaction demonstrations targeting two typical touch intention recognition tasks: directional control and multi-point identification. These experiments demonstrate the potential of MSSF in applications such as virtual control and music performance. In the first experiment, as shown in Figure S7 and Video S3 (Supporting Information), MSSF was sewn onto the user's forearm sleeve and folded into a square structure with a side length of ≈ 6 cm, forming a 2D touch control unit. The four corners of the square corresponded to the four movement directions ("up", "down", "left", and "right") of a game character. By continuously acquiring touch signals at different corners and leveraging the capacitance-based position recognition model established earlier, the system was able to accurately determine the specific touch location and map it to directional movement commands. To showcase this function, a "Sokoban" game was developed, in which the user controlled the character's movement by touching the four corners, enabling smooth navigation and successful task completion along a target path. The entire interaction process was responsive and accurate, fully demonstrating the high spatial resolution and real-time intention recognition capabilities of MSSF in touch-based directional input.

In the second experiment, as shown in Figure S8 (Supporting Information), we further evaluated the fine control capability of MSSF in continuous linear multi-point identification.

1616328, D. Downloaded from https://advanced.onlinelibrary.wiley.com/doi/10.1002/adfm.20324652 by Hangzhou Normal University, Wiley Online Library on [10/11/2025]. See the Terms and Conditions (https://onlinelibrary.wiejc.com/terms-and-conditions) on Wiley Online Library for rules of use; OA articles are governed by the applicable Creative Commons License

www.afm-journal.de

Specifically, a 12 cm-long MSSF (after folding) was linearly sewn onto the user's forearm sleeve, and seven equally spaced touch regions were defined along its length, each corresponding to a musical scale note: "do", "re", "mi", "fa", "so", "la", and "ti". By lightly touching different positions along the fiber surface, the system could accurately detect the relative distance between the touch point and the electrode, thereby triggering the playback of the corresponding note. To enhance user experience, a simple piano interface was developed. As shown in Video S4 (Supporting Information), when the user touched the fiber sequentially from the proximal to the distal end, the system generated the corresponding musical notes, completing the "do-re-mi..." scale sequence. Experimental results demonstrated excellent performance in seven-point resolution, response speed, and repeatable triggering consistency, enabling delay-free and error-free multipoint audio input. As shown in Video \$5 (Supporting Information), in a representative demonstration, the user performed the well-known children's song "Two Tigers" by sequentially tapping the defined touch regions on the MSSF. Each finger taps along the fiber triggered the corresponding musical note in real time, with the system accurately identifying the touch location and executing immediate audio feedback without noticeable latency. The consistent pitch and rhythm across repeated performances confirmed the high spatial resolution and signal stability of the sensor.

This verifies the feasibility of MSSF for future applications in multi-channel input recognition and embodied musical interaction. These two HMI demonstrations fully highlight the application potential of MSSF in complex touch intention recognition scenarios. Its excellent spatial resolution, rapid response speed, and high compatibility with sewable integration make it not only suitable as a fundamental touch unit in wearable virtual control systems, but also extendable to continuous multi-point input applications. Together, these features provide a novel implementation paradigm for intelligent fiber systems designed for immersive interaction.

2.4. Deep Learning-Enabled Touch Intention Decoding

The core of touch intention recognition lies in establishing a learnable mapping between user touch behavior and control commands, thereby enabling more natural and efficient HMI in immersive scenarios such as VR. To this end, as shown in Figure 3A, we developed a touch intention recognition system that integrated a flexible sensing structure with deep learning algorithms, enabling real-time acquisition and digital decoding of user handwriting trajectories based on MSSF. In terms of structural design, as illustrated in Figure S9 (Supporting Information), we adopted a biomimetic optimization strategy inspired by the spiral layout of spider webs in nature. The spiders use the least amount of mucus to weave their webs, with the most area coverage. The spiral structure within a spider web possesses excellent capabilities in vibration guidance and localization, allowing weak disturbances caused by prey to be rapidly directed to the center of perception, forming an efficient signal transmission pathway.[29,30] Unlike planar or linear fiber sensors that can only respond along a single axis, the spiral layout naturally introduces a 2D coordinate response. The radial and angular variations in capacitance allow the system to infer both the touch position and movement direction with higher spatial resolution. Inspired by this mechanism, we wove MSSF into a spiral configuration and sewed it onto the surface of wearable fabrics, thereby constructing a 2D touch network with wide-area sensing capability and directional discrimination.

To evaluate the spatial resolution capability of the spiral structure, we designed a continuous pressing experiment involving seven predefined touch points (L1-L7), as shown in Figure \$10A (Supporting Information). The results indicate that the output capacitance values initially decrease and then increase with changes in touch location, accurately reflecting the nonlinear distance variation between the touch points and the electrode terminal. This behavior aligns with the geometric regulation of sensing path length inherent to the spiral configuration. Furthermore, as shown in Figure S10B and Video S6 (Supporting Information), when the finger slides gradually along the spiral toward the electrode, the capacitance response continuously increases, demonstrating the system's strong continuity and stability in trajectorybased touch localization. In practical use, users slide their fingers along the surface of the spiral-structured MSSF to perform digit-writing gestures. The system captures dynamic capacitance changes in real time, producing a 1D time-series signal stream. This signal encodes multi-dimensional tactile information, including position, direction, and contact intensity, providing rich input for subsequent deep learning models.

To enable effective digit recognition, a custom dataset consisting of 10-digit classes (0–9) with a total of 200 samples (20 samples per class) was collected (Figure S11, Supporting Information) to train and evaluate the recognition model. As shown in Figures S12 and S13 (Supporting Information), we further performed cluster analysis using both t-distributed stochastic neighbor embedding (t-SNE) and dynamic time warping-based downsampled clustering to visualize the feature space and assess interclass separability. Digit classes form well-separated clusters in the 2D projection, demonstrating high inter-class discrimination and intra-class compactness. These results confirm that the extracted features are well-structured and suitable for downstream intention decoding.

To achieve high-accuracy and high-robustness digit intention recognition, we developed a dual-branch deep learning framework that integrates the feature extraction capability of a 1D convolutional neural network (1D-CNN) for time-series signals with structural priors from manually extracted peak features. This design improves both recognition accuracy and model generalizability.

The overall model architecture is shown in Figure 3B. Specifically, the raw waveform branch receives a 1D input sequence of length 3164, representing the capacitance time-series data. This branch passes through three modules, each consisting of a Conv1D layer followed by a MaxPooling1D layer, to progressively extract local temporal features and perform feature compression. The output is then flattened by a Flatten layer and encoded into a low-dimensional feature vector via a fully connected layer with 64 neurons. In parallel, the peak-feature branch takes a 13-dimensional manually extracted statistical feature vector (e.g., maximum value, inter-peak distance), which is processed by a Flatten layer and directly passed to the subsequent fusion stage. The outputs from both branches are concatenated into a unified

16163028, 0, Downloaded from https://advanced.onlinelibrary.wiley.com/doi/10.1002/adfm.202524652 by Hangzhou Normal University, Wiley Online Library on [10/11/2025]. See the Terms and Conditions (https://onlinelibrary.wiley

conditions) on Wiley Online Library for rules of use; OA articles are governed by the applicable Creative Commons License

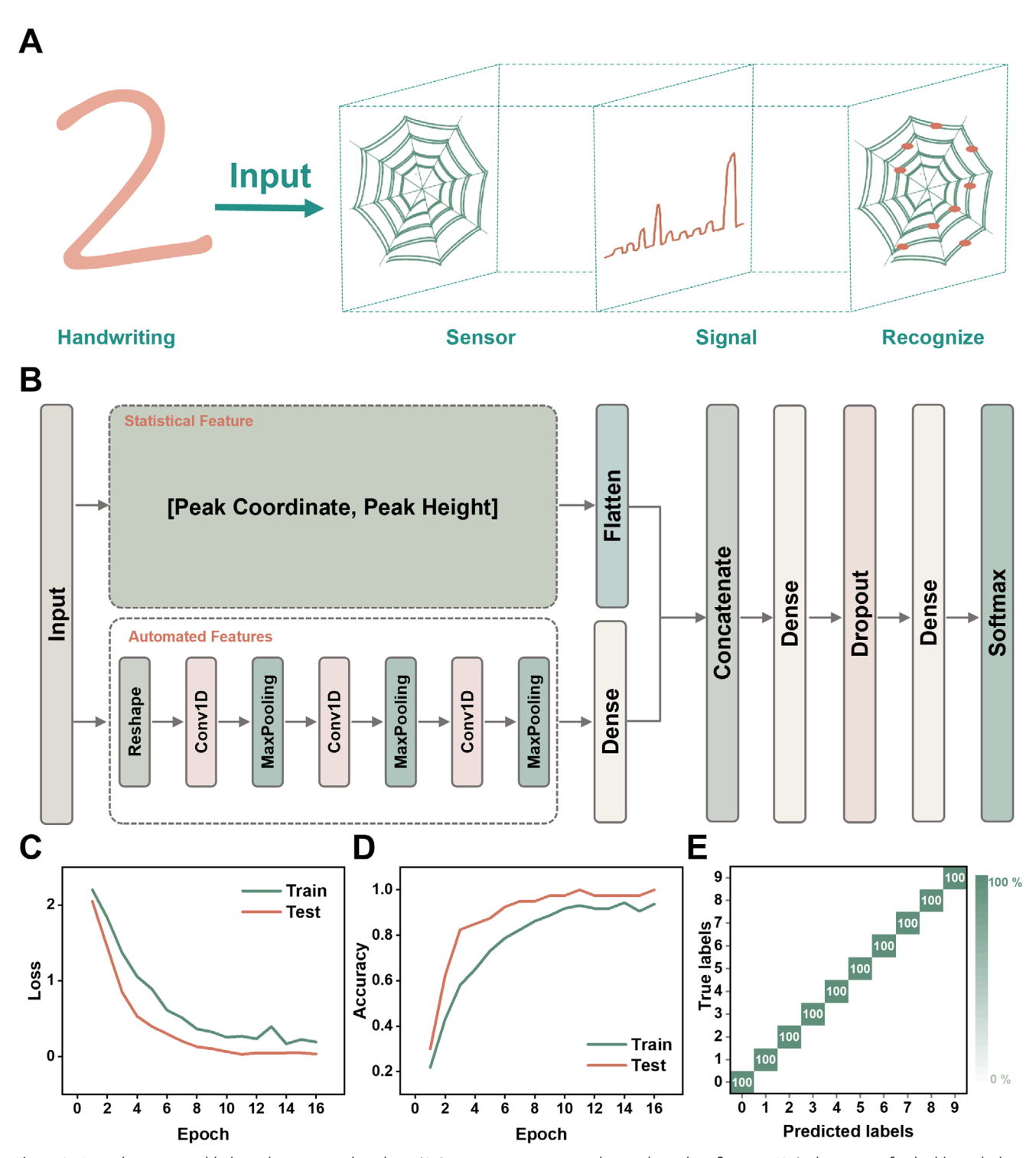


Figure 3. Deep learning-enabled touch intention decoding. A) Sensor array operation during digit identification. B) Architecture of a dual-branch deep learning framework. C) Training set and test set loss comparison. D) Training set and test set accuracy curves. E) Confusion matrix of recognition results.

feature vector and then passed through two fully connected layers (128 and 64 dimensions), with a Dropout layer inserted in between to mitigate overfitting. Finally, a softmax classifier outputs the probability distribution over 10-digit classes, enabling precise recognition of digit-writing intentions. Model training was con-

ducted using the cross-entropy loss function and optimized with the Adam optimizer. During training, the model exhibited good convergence in both accuracy and loss curves (Figure 3C,D), validating its learning capability and training stability under smallsample conditions.

16163028, 0, Downloaded from https://advanced.

onlinelibrary.wiley.com/doi/10.1002/adfm.202524652 by Hangzhou Normal University, Wiley Online Library on [10/11/2025]. See the Terms and Conditions (https://onlinelibrary.wiley.com/ten

-conditions) on Wiley Online Library for rules of use; OA articles are governed by the applicable Creative Commons License

www.afm-journal.de

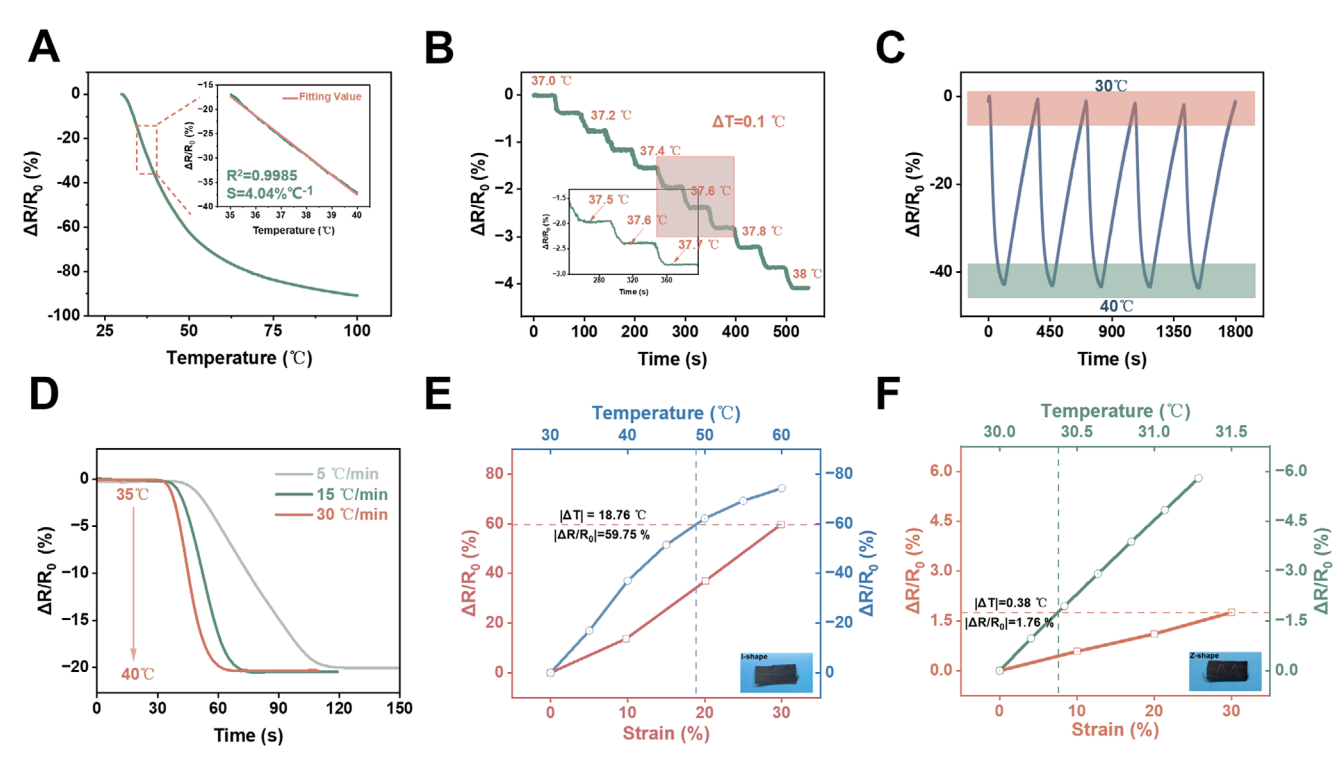


Figure 4. Accurate temperature detection based on MSSF. A) Real-time $\Delta R/R_0$ response of the sensor to temperatures ranging from 30 to 100 °C. The inset in (A) is the linear fitting of $\Delta R/R_0$ vs temperature in the range of 35–40 °C. B) $\Delta R/R_0$ as a function of the temperature kept at 37 °C and the increasing temperature from 37 to 38 °C with a temperature gradient of 0.1 °C. C) $\Delta R/R_0$ as a function of time during five heating-cooling cycles between 30 and 40 °C. D) $\Delta R/R_0$ as a function of time when the sensor was heated from 35 to 40 °C at different heating rates (5, 15, and 30 °C min⁻¹, respectively). The $\Delta R/R_0$ variation of "I"- (E), "Z"- (F) shaped sensors under temperature changes and $\Delta R/R_0$ variation of these sensors with strains in the range of 0 to 30%.

The final test results, presented in the form of a confusion matrix (Figure 3E), show that the model achieved 100% classification accuracy across the 10-digit test set, fully demonstrating the separability of MSSF-based tactile behavior signals and the reliability of the recognition model. These results confirm that the integration of the biomimetic spiral-structured MSSF with deep learning algorithms enables a tactile intention recognition system that combines high spatial resolution, high signal sensitivity, and high decoding accuracy. This system not only enables precise interpretation of dynamic touch behaviors such as digit writing, but also exhibits excellent adaptability to various environments and strong algorithmic extensibility. With its structural flexibility, intelligent recognition capability, and stable sensing performance, this platform provides a unified, real-time, and highly integrated perception-computation solution for intelligent wearable interaction systems in VR/AR applications.

2.5. Accurate Temperature Detection

In high-intensity interaction scenarios, users' physiological states, especially body temperature, often exhibit dynamic variations due to physical exertion or emotional fluctuations. To enable real-time tracking and accurate monitoring of temperature changes, a flexible temperature sensing unit with high sensitivity and resolution was integrated into MSSF, and its resistive response behavior and sensing mechanism were systematically

investigated. The temperature-sensing functionality is based on the temperature-dependent ionic conductivity of the ionic liquid. Specifically, the degree of dissociation of the ionic liquid in MSSF increases with temperature, enhancing the mobility of ions, elevating the charge carrier concentration and transport rate, and thereby inducing a predictable change in the overall resistance of the fiber. This mechanism can be quantitatively described by the Vogel–Tammann–Fulcher (VTF) equation:

$$\sigma\left(T\right) = \sigma_0 \exp\left(-\frac{B}{T - T_0}\right) \tag{5}$$

Here, $\sigma(T)$ represents the ionic conductivity, and σ_0 , B, and T_0 are constants determined by the material composition. As temperature increases, intermolecular energy barriers are reduced and ion migration channels become more accessible, leading to an increase in overall conductivity and a corresponding decrease in resistance—exhibiting a typical negative temperature coefficient (NTC) behavior.

Figure 4A presents the temperature response of MSSF over the range of 30–100 °C. The $\Delta R/R_0$ value decreases continuously with rising temperature, reflecting a stable NTC response characteristic. Notably, within the physiological temperature range of 35–40 °C, the sensor exhibits a sensitivity of up to 4.04% °C⁻¹ (inset of Figure 4A), enabling high-precision resolution of subtle temperature changes. This makes it suitable for VR-related

1616928, 0, Downloaded from https://advanced.onlinelibrary.wiley.com/doi/10.1002adfm.20254655 by Hangzbou Normal University, Wiley Online Library on [10.11/2025]. See the Terms and Conditions (https://onlinelibrary.wiley.com/terms-and-conditions) on Wiley Online Library for rules of use; OA arches are governed by the applicable Cerative Commons.

applications such as activity-state monitoring and thermal stress warning.

To further verify the temperature sensing resolution and stability of MSSF, a stepwise heating test with 0.1 °C increments was conducted (Figure 4B). The results show that the $\Delta R/R_0$ curve exhibits a stable decreasing trend during gradual temperature elevation and maintains consistent output at each temperature plateau, indicating that the sensor possesses a high resolution of 0.1 °C and is highly reliable and resistant to external disturbances. Repeatability and response consistency are critical for the long-term reliability of temperature sensors.

Figure 4C shows the results of five consecutive heatingcooling cycles performed within the 30–40 °C range. The $\Delta R/R_0$ curves for all cycles nearly overlap, demonstrating excellent response repeatability and structural stability under dynamic thermal loading conditions. In addition, as shown in Figure 4D, we evaluated the sensor's performance under different heating rates (5, 15, and 30 °C min⁻¹). The results indicate that the magnitude of $\Delta R/R_0$ remained nearly unchanged regardless of the heating rate, reflecting good rate-independence and dynamic response stability. These characteristics make MSSF well-suited for capturing temperature fluctuations and providing real-time feedback in various application scenarios. In conclusion, MSSF not only achieves structural integration for wearable applications but also combines high sensitivity, high resolution, and excellent stability in performance. These advantages make it well-suited for practical use in body temperature monitoring, physiological feedback regulation, and thermal safety alerting in VR/AR environments, thereby offering an additional critical sensing channel for immersive virtual interaction systems.

To address the influence of strain on temperature sensing in fiber sensors, we designed two unique integrated architectures for textiles: the "I"-shaped configuration and the "Z"-shaped configuration, evaluating their respective relative resistance-strain response characteristics (as shown in Figure S14A, Supporting Information). Figure S14B (Supporting Information) compares the $\Delta R/R_0$ -strain curves of the two structural fiber sensors. It can be observed that the $\Delta R/R_0$ of the "I"-shaped sensor increases linearly with strain, where 50% strain leads to ≈114% change in relative resistance. In contrast, the "Z"-shaped sensor exhibits only about a 2.96% increase in $\Delta R/R_0$ under 50% strain. This indicates that the influence of 50% strain on the "Z"-shaped sensor is minimal and nearly negligible, allowing the sensor to respond solely to ambient temperature.

To evaluate the interference of strain on the temperature response of these two differently shaped sensors, we compared their $\Delta R/R_0$ variations induced by temperature changes and a 30% strain change. For the "I"-shaped sensor, the absolute $\Delta R/R_0$ change caused by 30% strain stimulation reaches 59.75%, equivalent to a temperature change of 18.76 °C (Figure 4E). In comparison, as shown in Figure 4F, the "Z"-shaped sensor under 30% strain stimulation produces an absolute $\Delta R/R_0$ value of 1.76%, corresponding to a temperature change of 0.38 °C. These results demonstrate that the "Z"-shape geometric structure design can effectively eliminate strain interference caused by human motion when the fiber functions as a temperature sensor.

2.6. High-Resolution, Wide-Range Motion Capture

In VR interactive systems, as shown in **Figure 5**A, the user's body movements are increasingly replacing traditional external controllers as the primary form of input. This requires real-time acquisition of dynamic deformations, such as joint flexion and limb extension, to drive smart devices, provide system feedback, or enable task control. Such input modalities impose stringent performance requirements on wearable strain sensors. An ideal strain sensor must cover a wide dynamic range, from subtle fingertip motions to large-scale limb movements, while maintaining highresolution output in the low-strain region and delivering stable and reliable performance under long-term, multi-cycle operation. Furthermore, fast response and recovery capabilities are essential to ensure a smooth and seamless interaction experience. To this end, we systematically evaluated the strain-sensing performance of MSSF, including its linear response under large deformation, detection limit for small strains, cyclic stability under dynamic loading, and response time under instantaneous strain stimuli, to validate its overall adaptability and engineering feasibility for wearable motion capture systems.

The strain-sensing behavior of MSSF arises from the coupling relationship between electrical resistance (R) and strain (ϵ), which is jointly governed by the ionic conduction mechanism of the material and the evolution of its microstructure. According to the fundamental definition of resistance:

$$R = \rho \frac{L}{A} \tag{6}$$

where ρ is the resistivity, *L* is the fiber length, and *A* is the crosssectional area of the ionogel fiber. Assuming that the fiber maintains constant volume during stretching, and defining the strain

$$\varepsilon = \frac{L' - L_0}{L_0} \tag{7}$$

Where L_0 is the initial length. The resistance change in MSSF is mainly attributed to two synergistic mechanisms: 1) As the IL/TPU fiber is stretched, its length increases while crosssectional area decreases, geometrically contributing to an increase in resistance. More importantly, the extended fiber length elongates the ion transport pathways. This increased migration distance raises the likelihood of ionic collisions and scattering, thereby decreasing ionic transport efficiency and increasing the material's intrinsic resistivity ρ ; 2) Under tensile strain, TPU molecular chains progressively uncoil and relax, loosening the polymer network. This expansion increases free volume and reduces steric hindrance, thus lowering the barrier for ion movement. The resulting improvement in ionic mobility partially offsets the resistivity increase caused by path elongation, and may even reduce ρ under certain strain regimes.^[34,35]

The variation of length and cross-sectional area with strain can be derived as:

$$L' = L_0 \left(1 + \varepsilon \right) \tag{8}$$

$$A' = \frac{A_0}{1 + \varepsilon} \tag{9}$$

16163028, 0, Downloaded from https://advanced.onlinelibrary.wiley.com/doi/10.1002/adfm.202524652 by Hangzbou Normal University, Wiley Online Library on [10/11/2025]. See the Terms and Conditions (https://onlinelibrary.wiley.com/doi/10.1002/adfm.202524652 by Hangzbou Normal University, Wiley Online Library on [10/11/2025]. See the Terms and Conditions (https://onlinelibrary.wiley.com/doi/10.1002/adfm.202524652 by Hangzbou Normal University, Wiley Online Library on [10/11/2025]. See the Terms and Conditions (https://onlinelibrary.wiley.com/doi/10.1002/adfm.202524652 by Hangzbou Normal University, Wiley Online Library on [10/11/2025]. See the Terms and Conditions (https://onlinelibrary.wiley.com/doi/10.1002/adfm.202524652 by Hangzbou Normal University, Wiley Online Library on [10/11/2025]. See the Terms and Conditions (https://onlinelibrary.wiley.com/doi/10.1002/adfm.202524652 by Hangzbou Normal University, Wiley Online Library on [10/11/2025]. See the Terms and Conditions (https://onlinelibrary.wiley.com/doi/10.1002/adfm.202524652 by Hangzbou Normal University, Wiley Online Library on [10/11/2025]. See the Terms and Conditions (https://onlinelibrary.wiley.com/doi/10.1002/adfm.202524652 by Hangzbou Normal University, Wiley Online Library on [10/11/2025]. See the Terms and Conditions (https://onlinelibrary.wiley.com/doi/10.1002/adfm.202524652 by Hangzbou Normal University, Wiley Online Library on [10/11/2025]. See the Terms and Conditions (https://onlinelibrary.wiley.com/doi/10.1002/adfm.202524652 by Hangzbou Normal University, Wiley Online Library on [10/11/2025]. See the Terms and Conditions (https://onlinelibrary.wiley.com/doi/10.1002/adfm.202524652 by Hangzbou Normal University, Wiley Online Library.wiley.com/doi/10.1002/adfm.202524652 by Hangzbou Normal University, Wiley Online Library.wiley.com/doi/10.1002/adfm.202524652 by Hangzbou Normal University, Wiley Online Library.wiley.com/doi/10.1002/adfm.202524652 by Hangzbou Normal University (https://onlinelibrary.wiley.com/doi/10.1002/adfm.202524652 by Hangzbou

and-conditions) on Wiley Online Library for rules of use; OA articles are governed by the applicable Creative Commons License

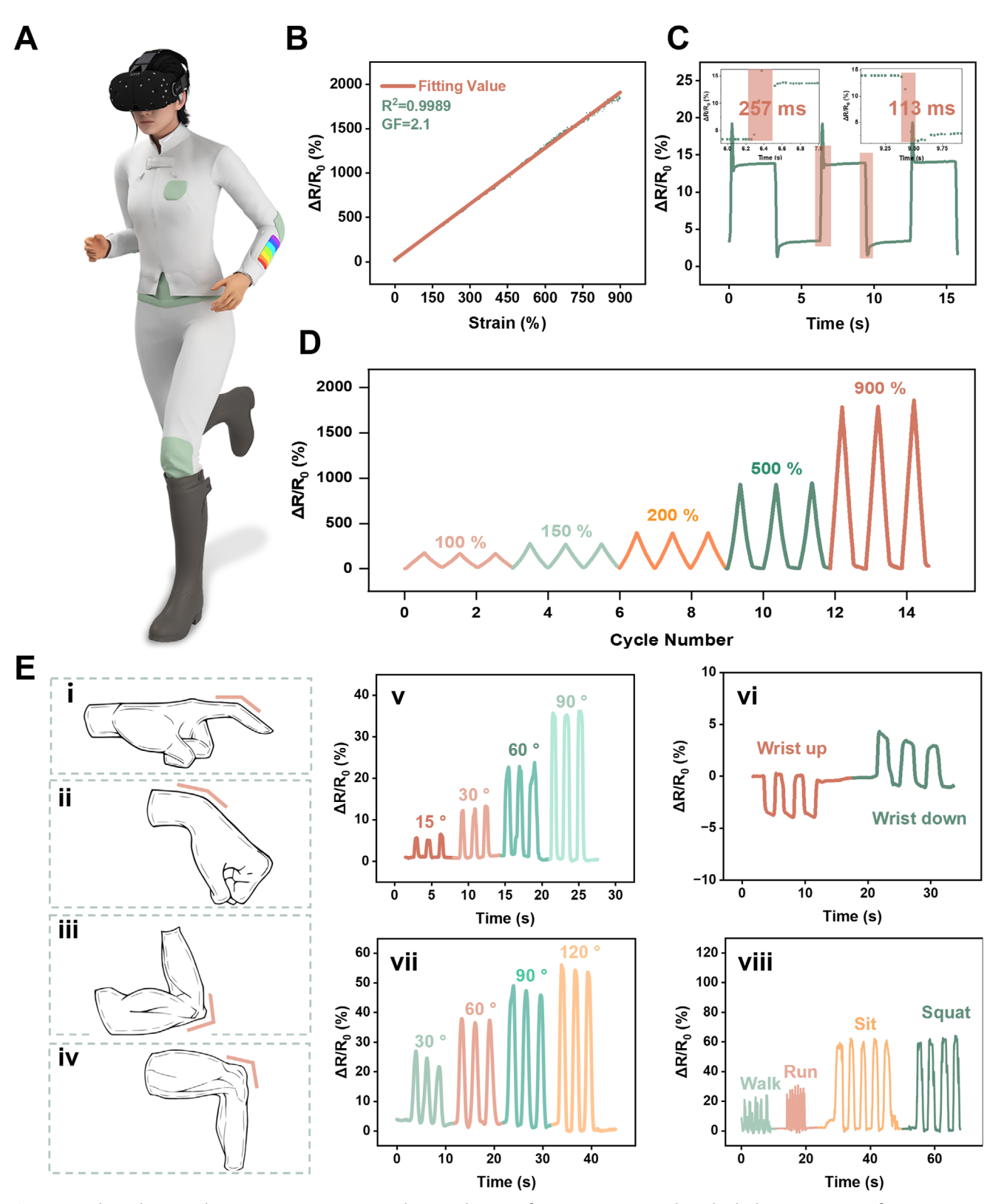


Figure 5. High-resolution, wide-range motion capture. A) Schematic diagram of MSSF integration at the individual joints. B) Curve of $\Delta R/R_0$ vs strain for the strain sensor upon uniaxial stretching. C) Measured response time and recovery time of the sensor at 0.1% strain. D) $\Delta R/R_0$ response of the sensor to 100–900% strain over three stretch/release cycles. E) Demonstration experiments: (i, v) finger, (ii, vi) wrist, (iii, vii) elbow, and (iv, viii) knee, showing a schematic of sensor placement and corresponding $\Delta R/R_0$ signal responses.

FUNCTIONAL ___ MATERIALS 1616328, D. Downloaded from https://advanced.onlinelibrary.wiley.com/doi/10.1002/adfm.20324652 by Hangzhou Normal University, Wiley Online Library on [10/11/2025]. See the Terms and Conditions (https://onlinelibrary.wiejc.com/terms-and-conditions) on Wiley Online Library for rules of use; OA articles are governed by the applicable Creative Commons License

Assume that the relationship between the resistivity of the fiber and the strain is according to the following relationship under the influence of the above two factors:

$$\rho' = \frac{\rho_0}{1 + \varepsilon} \tag{10}$$

Substituting Equations (8–10) into Equation (6), the quantitative relationship between resistance and strain can be expressed

$$R' = \frac{\rho_0}{1+\varepsilon} L_0 (1+\varepsilon) \frac{1+\varepsilon}{A_0} \tag{11}$$

$$R' = \rho_0 \frac{L_0}{A_0} \left(1 + \varepsilon \right) \tag{12}$$

where R_0 and ρ_0 denote the initial resistance and resistivity, respectively. The combined effect of these mechanisms allows MSSF to maintain a stable and predictable resistive response across an ultrawide strain range.

Figure 5B shows the strain response curve of MSSF under uniaxial stretching from 0 to 900%. The results indicate that the device exhibits excellent linearity across the entire strain range, with a fitted coefficient of determination (COD) of 0.9989 and a GF of 2.1, satisfying the requirements for linear input in high-dynamic interaction scenarios. More importantly, MSSF maintains high linearity and a wide dynamic range while also demonstrating high resolution in detecting small deformations. Figure 5C presents the response speed test results. Under a loading rate of 1000 mm min⁻¹ and a small strain input of 0.1%, the sensor exhibited rapid response capability, with response and recovery times of 257 and 113 ms, respectively. This millisecond-level responsiveness provides strong support for real-time control applications. As shown in Figure S15A (Supporting Information), the minimum detectable strain reaches as low as 0.1%, enabling the precise capture of subtle human motions such as initial finger bending. This high sensitivity is attributed to the uniform dispersion of the ionic liquid within the TPU matrix, which forms a continuous and responsive ion transport pathway, ensuring detectable and consistent resistance changes even under extremely low strain conditions. Regarding device stability, Figure \$15B (Supporting Information) and Figure 5D show the results of three consecutive tensile-release cycles conducted under different strain amplitudes ranging from 5% to 900%. The resistance signals exhibit minimal fluctuation, indicating excellent cyclic repeatability. Further stepwise strain testing (Figure S16, Supporting Information) was performed to verify the response consistency under complex loading conditions. When the strain was increased in 50% increments up to 200%, the $\Delta R/R_0$ response peaks grew in a regular manner, and the signals in the second cycle were fully reproduced, demonstrating outstanding dynamic stability. In addition, a 1000-cycle stretch-release test with a 30% strain amplitude was conducted (Figure S17, Supporting Information). The results show negligible baseline drift and highly consistent peak amplitudes throughout the entire test, further confirming the excellent durability and repeatability of MSSF under long-term cyclic mechanical loading.

Adv. Funct. Mater. 2025, e24652

As shown in Figure S18A (Supporting Information), we systematically characterized the sensor's strain-sensing performance at different constant temperatures (30, 40, 45, 55 °C). The strain sensitivity demonstrated high stability and consistency across these temperature conditions. This finding indicates that temperature variation primarily induces a vertical shift in the initial resistance baseline without significantly altering the strain sensitivity (i.e., the slope of the curve) within the above temperature range. After retrieving the pre-stored baseline resistance value R_0 corresponding to the measured temperature T from a database (Figure S18B, Supporting Information), the $\Delta R/R_0$ value can be directly used to calculate the suffered strain, thereby effectively eliminating the crosstalk caused by temperature variations.

Figure 5E comprehensively demonstrates the wearable integration of MSSF at multiple representative human joint regions-namely the fingers, wrists, elbows, and knees-and its dynamic strain response performance, validating its motion capture capability across diverse scenarios. In the fingerbending test (Figure 5E(i)), MSSF was affixed to the dorsal side of the finger. As the finger was bent incrementally at angles of 15°, 30°, 60°, and 90° (Figure 5E(v)), the sensor's resistance increased monotonically with bending angle. The response curves were stable, with no noticeable signal drift or noise, indicating high sensitivity and fine resolution for detecting subtle joint movements. Wrist monitoring results are shown in Figure 5E(ii,vi), where the sensor was attached to the back of the wrist. Upward and downward wrist movements were performed during testing, both of which induced distinct resistance changes. The signal amplitude was strongly correlated with the degree of motion, reflecting the consistent responsiveness of MSSF to both amplitude variation and directional switching-features wellsuited for applications in gesture localization and posture

For elbow monitoring (Figure 5E(iii,vii)), MSSF was used to detect flexion at 30°, 60°, 90°, and 120°. The resistance response exhibited a highly linear relationship with elbow angle, and the signal amplitude increased clearly and proportionally, further confirming the sensor's accuracy and structural adaptability under moderate to large deformation conditions. Figure 5E(iv,viii) further presents the application of MSSF at the knee joint. Tests covered typical daily activities, including walking, running, sitting, and squatting. The sensor produced stable resistance curves under all conditions, and the waveform patterns corresponding to different motions were clearly distinguishable. These results demonstrate MSSF's capability in decoding complex motion patterns, making it particularly suitable for wearable applications in gait recognition, activity monitoring, and immersive interactive feedback. Taken together, MSSF is able to capture resistance signal variations in real time with high sensitivity and resolution, whether for small-angle finger movements or large-range knee flexion and extension. This capability is particularly critical for motion control in VR/AR-based virtual interactions, as it not only significantly enhances the accuracy and naturalness of action recognition but also provides a reliable perceptual foundation for immersive experience at the system level.

www.advancedsciencenews.com



1616328, D. Downloaded from https://advanced.onlinelibrary.wiley.com/doi/10.1002/adfm.20324652 by Hangzhou Normal University, Wiley Online Library on [10/11/2025]. See the Terms and Conditions (https://onlinelibrary.wiejc.com/terms-and-conditions) on Wiley Online Library for rules of use; OA articles are governed by the applicable Creative Commons License

www.afm-journal.de

2.7. Deep Learning-Driven Gesture Recognition and Robotic Control

To enable intelligent gesture-based control, as shown in Figure S19A (Supporting Information), we integrated MSSF onto the joints of five fingers and developed a CNN-based system that forms a closed-loop pipeline from gesture perception to command execution. As shown in Figure 6A, MSSF continuously captures five-channel strain signals corresponding to finger movements, with each static gesture generating a distinct resistance pattern. The dataset includes 10 gestures classes; each performed 20 times by five participants. All collected five-channel signals were organized into 2D tensors and used to train and evaluate the recognition model, with 80% of the data allocated for training and 20% for testing.

To assess the discriminability of the gesture features, we performed t-SNE dimensionality reduction on the extracted representations. As shown in Figure 6B, the results revealed clear class-wise clustering in the embedded 2D space. Quantitatively, the clustering quality was evaluated using the Adjusted Rand Index (ARI) and Normalized Mutual Information (NMI), which reached 0.6286 and 0.8180, respectively, confirming strong intra-class compactness and inter-class separability of the MSSF-based gesture signals. The CNN architecture is shown in Figure 6C. It employs a progressively deepened structure to efficiently extract local temporal and inter-channel features. The first two convolutional layers use 16 and 32 filters of size 3 x 1 to extract time-domain features, followed by two 2 × 1 max-pooling layers for dimensionality reduction and improved robustness. A third convolutional layer with 64 filters of size 2 × 2 captures deeper spatial correlations. After flattening, the extracted features are passed through fully connected layers and finally mapped to a 10-class softmax output vector representing gesture probabilities. The model uses rectified linear unit (ReLU) activations, is trained with a softmax cross-entropy loss function, and optimized via the Adam optimizer.

As shown in Figure 6D,E, the network exhibited rapid and stable convergence during training. The validation accuracy surpassed 95% within just six epochs and steadily improved to reach 100% by the 12th epoch. Correspondingly, the training loss decreased from an initial value of 2.24 to below 0.01, while the validation loss dropped from 1.99 to 0.01, indicating excellent fitting without signs of overfitting. The gesture recognition performance of the MSSF-based system was quantitatively evaluated using precision, recall, and F1-score across all 10 gesture classes. As shown in the classification report (Table S2, Supporting Information), the model achieved perfect scores of 1.00 in all three metrics for every gesture category. The overall accuracy, macro average, and weighted average were all 1.00, indicating flawless classification performance on the test set. This outstanding performance is further corroborated by the confusion matrix (Figure 6F), where all predictions lie precisely on the diagonal, indicating 100% correct classification for each gesture without any mislabeling. These results confirm the exceptional capability of the proposed system to reliably distinguish among diverse gesture patterns with zero misclassification. The consistent perclass performance further demonstrates the model's robustness across gesture categories with varying sample sizes, validating the high quality of both the MSSF signal acquisition and the deep learning model architecture.

To further evaluate the generalization capability of the trained deep learning model in cross-user scenarios, we conducted additional validation. In this test, three participants who were not involved in model training each performed ten predefined gestures ten times. The pretrained model, without retraining or fine-tuning, achieved recognition accuracies of 94%, 98%, and 99%, respectively (Figure S19B, Supporting Information). These results indicate that the model maintains high robustness and adaptability when applied to unseen users, demonstrating its strong potential for practical deployment in real-world HMI systems. The minor accuracy variation among different individuals may stem from personal differences in gesture amplitude and execution speed, suggesting that future work could incorporate adaptive calibration or transfer learning to further enhance user-independent recognition performance.

Based on the classification results, we implemented a real-time mapping from gesture recognition to robotic hand control, achieving a complete closed-loop interaction. As shown in Figure 6G and Video S7 (Supporting Information), when the user performs a predefined gesture while wearing the MSSF, the system classifies the input in real time and sends corresponding commands to drive the robotic hand. For example, an "openhand" gesture triggers synchronous extension of all five robotic fingers, demonstrating smooth and low-latency response. This system not only showcases the potential of MSSF in gesture perception and recognition but also validates its effectiveness when coupled with deep learning for high-accuracy, real-time interactive control.

Looking forward, the deep learning-enabled gesture-to-command paradigm established here opens new avenues for MSSF in advanced HMI. Future developments could extend beyond direct robotic mimicry to semantic-level control, where recognized gestures trigger predefined actions in complex scenarios. In immersive VR/AR environments, this could include opening virtual menus, manipulating 3D objects, or navigating virtual spaces through intuitive hand signals. In assistive technologies, MSSF could be adapted to interpret sign language from individuals with speech or hearing impairments, converting gestures into audible speech or digital text for real-time communication. It offers a scalable solution for next-generation wearable gesture interfaces and intelligent robotic control platforms.

3. Conclusion

This study presents an ionogel-based multifunctional sensing single-fiber that integrates touch, temperature, and strain sensing into a unified multifunctional platform through coordinated material and structural design. The sensor establishes a neuromorphic input pathway within a flexible, wearable fiber form, enabling high-resolution, rapid, and robust multifunctional signal acquisition. MSSF supports diverse interaction modes, including touch intention decoding, motion tracking, and thermal monitoring, and can be seamlessly integrated into garments for wearable VR/AR applications. Coupling sensory hardware with AI-driven signal interpretation, it provides a deployable unit for closed-loop "perception-computation-feedback" systems.

ons) on Wiley Online Library for rules of use; OA articles are governed by the applicable Creative Commons License

www.afm-journal.de

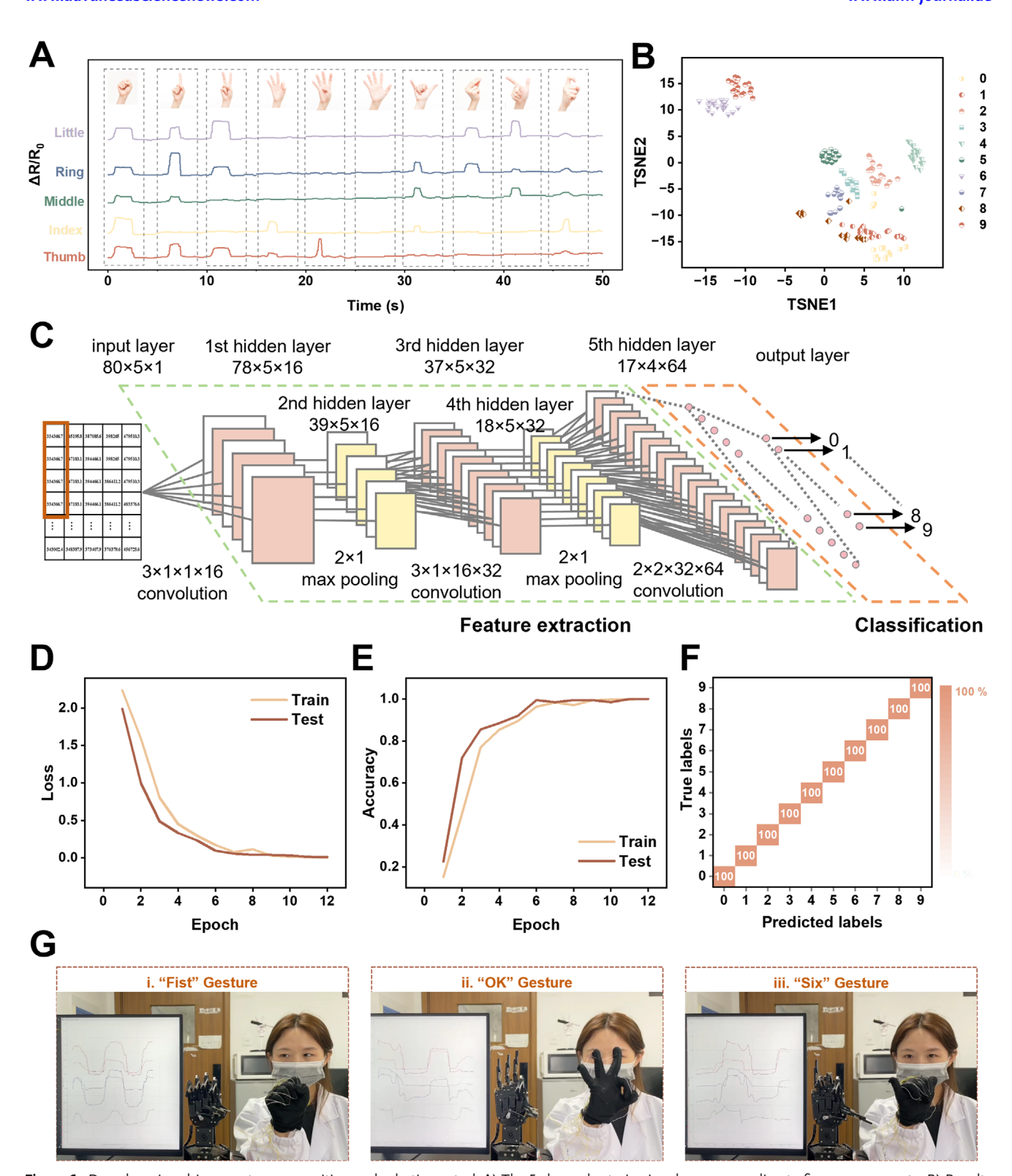


Figure 6. Deep learning-driven gesture recognition and robotic control. A) The 5 channels strain signals corresponding to finger movements. B) Results of t-SNE downscaling of extracted representations. C) The CNN architecture. D) Training set and test set loss comparison. E) Training set and test set accuracy curves. F) Confusion matrix for 10 gesture recognition results. G) Demonstration of a robotic hand tracking user gesture.

www.advancedsciencenews.com



www.afm-journal.de

Overall, this work demonstrates the integration potential of single-fiber formats for intelligent sensing and lays the foundation for scalable, distributed, and adaptive human-machine interfaces in next-generation wearable electronics.

4. Experimental Section

Materials: Thermoplastic polyurethane (TPU, Elastollan 1185A) was purchased from BASF Co., Ltd. The ionic liquid (IL), 1-ethyl-3-methylimidazolium bis (trifluoromethylsulfonyl)imide ([EMIm][NTf₂], purity >99%), was obtained from Shanghai Chengjie Chemical Co., Ltd. Tetrahydrofuran (THF, 99%) was supplied by Sinopharm Chemical Reagent Co., Ltd

Preparation of IL/TPU lonogels and 3D Printed lonogel Fibers: To prepare the IL/TPU ionogel precursor, 10 g of TPU was first dissolved in 100 mL of THF by magnetic stirring at 500 rpm for 4 h. Then, 10 g of [EMIm][NTf₂] was added to the solution to achieve a TPU:IL mass ratio of 1:1. The mixture was further stirred at room temperature for 3 h and ultrasonicated for 30 min (300 W, 40 kHz) to obtain a homogeneous solution. The resulting solution was cast onto a metal tray and left to dry for 12 h to allow full THF evaporation and film formation. The dried films were cut into pellets and loaded into a melt-extrusion 3D printer (Piocreat 3D, Shenzhen, China). Fibers of various diameters (0.4, 0.6, 0.8, 1.0 mm) were fabricated under a nozzle temperature of 180 °C and an extrusion speed of 40 mm s⁻¹ by changing the nozzle diameter accordingly.

Fabrication of the MSSF Device: To construct the multifunctional sensor (MSSF), IL/TPU fibers with lengths of 2–3 cm was used to fabricate strain and temperature sensors by attaching electrodes at both ends. For touch sensing, a longer fiber (\approx 30 cm) adopts a folded-parallel configuration, with electrodes affixed at both ends to form a symmetric capacitive sensing unit.

Structural Characterization and Electrical Performance Evaluation: The surface and cross-sectional morphologies of the IL/TPU ionogel fibers were characterized using scanning electron microscopy (SEM, Hitachi S-4800, 5 kV, Japan). Elemental mapping of the fiber cross-section was performed using energy-dispersive X-ray spectroscopy (EDS, Oxford Ultim Max170) integrated with SEM (ZEISS Sigma 500). Strain sensing performance was evaluated using a universal testing machine (INSTRON 5966, USA) equipped with a digital multimeter (TH 2832, Tonghui, China). Temperature-sensing behavior was analyzed using a hot-stage polarizing microscope (INSTEC HCS302), also coupled with a digital multimeter. Electrode processing with multifunctional flexible electronic printer (DB100, Prtronic, Shanghai Mifang Electronic Technology Co., LTD). Touch sensing signals were measured using a precision digital multimeter (DMM 7510, KEITHLEY, USA).

Touch Intention Recognition: The touch intention dataset was acquired by recording time-series capacitive signals from the MSSF spiral sensor during digit-writing tasks. Data were collected for 10 classes (digits 0–9), with 20 samples per class. The raw capacitive signals and manually extracted peak features were stored as NumPy arrays. During training, the model utilized a dual-input architecture with waveform and peak-value branches. The model was compiled using the Adam optimizer and trained with the following parameters: batch size of 32, 30 epochs, early stopping (patience = 5), and learning rate reduction on plateau (factor = 0.5, minimum LR = $1e^{-5}$). Validation accuracy and loss were monitored during training.

Gesture Recognition and Robotic Control: For gesture classification, MSSF sensors were sewn onto the knuckles of five fingers to collect five-channel resistance signals for 10 static hand gestures. Each gesture was performed 20 times by five participants, yielding a balanced dataset. The collected data were reshaped into 2D tensors and used to train a CNN. The model was compiled using Adam optimizer and sparse categorical cross-entropy loss. A combination of early stopping, learning rate adjustment, and accuracy-based early termination was implemented to ensure efficient training.

Ethics Statement: All human-related experiments in this study involved healthy adult volunteers wearing textile-integrated sensing systems

placed over clothing, with no direct contact with bare skin or any invasive procedure. No personal, biometric, or identifiable data was recorded. Therefore, approval from an ethics committee was not required. All participants gave informed consent prior to participation and demonstration.

Supporting Information

Supporting Information is available from the Wiley Online Library or from the author

Acknowledgements

This work was supported by the Natural Science Fund of Zhejiang Province (LRG25E030003) and the National Natural Science Foundation of China (52273070).

Conflict of Interest

The authors declare no conflict of interest.

Author Contributions

X.C., J.Z., and J.H. contributed equally to this work. J.H. and Y.Z. conceived the concept of the project. J.Z. and J.H. designed the research and wrote the first manuscript version. X.C., J.Z., and J.H. performed the experiments and analyzed the results. J.H. and Y.Z. helped with the theoretical model analysis. J.L. and L.N. helped revise the manuscript. Y.Z. supervised the research and manuscript preparation. All authors participated in the production of the final manuscript.

Data Availability Statement

The data that support the findings of this study are available from the corresponding author upon reasonable request.

Keywords

flexible sensor, human-machine interaction, machine learning, single-fiber

Received: September 17, 2025 Revised: October 22, 2025 Published online: 1616928, 0, Downloaded from https://advanced.onlinelibrary.wiley.com/doi/10.1002adfm.20254655 by Hangzhou Normal University, Wiley Online Library on [10.11.12025]. See the Terms and Conditions (https://onlinelibrary.wiley.com/terms-and-conditions) on Wiley Online Library for rules of use; OA articles are governed by the applicable Ceravive Commons

- [1] H. Cho, I. Lee, J. Jang, J. Kim, H. Lee, S. Park, G. Wang, Nat. Electron. 2023, 6, 619.
- [2] Y. Liu, C. Yiu, Z. Song, Y. Huang, K. Yao, T. Wong, J. Zhou, L. Zhao, X. Huang, S. K. Nejad, M. Wu, D. Li, J. He, X. Guo, J. Yu, X. Feng, Z. Xie, X. Yu, Sci. Adv. 2022, 8, abl6700.
- [3] X. Yu, Z. Xie, Y. Yu, J. Lee, A. VazquezGuardado, H. Luan, J. Ruban, X. Ning, A. Akhtar, D. Li, B. Ji, Y. Liu, R. Sun, J. Cao, Q. Huo, Y. Zhong, C. Lee, S. Kim, P. Gutruf, C. Zhang, Y. Xue, Q. Guo, A. Chempakasseril, P. Tian, W. Lu, J. Jeong, Y. Yu, J. Cornman, C. Tan, B. Kim, et al., *Nature* 2019, 575, 473.
- [4] F. Wen, Z. Zhang, T. He, C. Lee, Nat. Commun. 2021, 12, 5378.
- [5] P. Tan, X. Han, Y. Zou, X. Qu, J. Xue, T. Li, Y. Wang, R. Luo, X. Cui, Y. Xi, L. Wu, B. Xue, D. Luo, Y. Fan, X. Chen, Z. Li, Z. L. Wang, Adv. Mater. 2022, 34, 2200793.

ADVANCED
FUNCTIONAL
__MATERIALS

16163028, 0, Downloaded from https

onlinelibrary.wiley.com/doi/10.1002/adfm.202524652 by Hangzhou Normal University, Wiley Online Library on [10/11/2025]. See the Terms

and Conditions

(https://onlinelibrary.

on Wiley Online Library for rules of

use; OA articles

s are governed by the applicable Creative

- [6] Z. Ma, S. Yang, Y. Shi, Y. Fu, K. Wang, G. Xiao, B. Zou, Angew. Chem., Int. Ed. 2024, 63, 202406015.
- [7] W. Wang, Y. Jiang, D. Zhong, Z. Zhang, S. Choudhury, J. Lai, H. Gong, S. Niu, X. Yan, Y. Zheng, C. Shih, R. Ning, Q. Lin, D. Li, Y. Kim, J. Kim, Y. Wang, C. Zhao, C. Xu, X. Ji, Y. Nishio, H. Lyu, J. B. H. Tok, Z. Bao, Science 2023, 380, 735.
- [8] Z. Sun, M. Zhu, X. Shan, C. Lee, Nat. Commun. 2022, 13, 5224.
- [9] J. Qi, L. Yu, E. T. Khoo, K. W. Ng, Y. Gao, A. W. C. Kow, J. C. Yeo, C. T. Lim, Nat. Electron. 2024, 7, 1098.
- [10] X. Yu, Y. Fang, X. Sun, Y. Xie, C. Liu, K. Wang, G. Xiao, B. Zou, Angew. Chem., Int. Ed. 2024, 63, 202412756.
- [11] Y. Luo, C. Liu, Y. J. Lee, J. DelPreto, K. Wu, M. Foshey, D. Rus, T. Palacios, Y. Li, A. Torralba, W. Matusik, Nat. Commun. 2024, 15, 868.
- [12] Z. Liu, X. Hu, R. Bo, Y. Yang, X. Cheng, W. Pang, Q. Liu, Y. Wang, S. Wang, S. Xu, Z. Shen, Y. Zhang, Science 2024, 384, 987.
- [13] W. Zhao, G. Xiao, S. Qiu, Y. Shang, Y. Qin, J. Yang, J. Wang, J. Ning, Y. Fang, Q. Dong, Z. Liu, S. Li, J. Gao, B. Zou, Angew. Chem., Int. Ed. 2025, 64, 202504913.
- [14] K. Kim, J. Hong, K. Bae, K. Lee, D. J. Lee, J. Park, H. Zhang, M. Sang, J. E. Ju, Y. U. Cho, K. Kang, W. Park, S. Jung, J. W. Lee, B. Xu, J. Kim, K. J. Yu, Sci. Adv. 2024, 10, adr 1099.
- [15] J. Huang, Y. Sun, Y. Jiang, J. A. Li, X. Sun, X. Cao, Y. Zheng, L. Pan, Y. Shi, SmartMat 2025, 6, 1325.
- [16] Z. Xiong, J. Huang, J. Chen, Z. Liu, Y. Zhu, G. Sui, Z. Liu, Chem. Eng. J. 2025, 503, 158359.
- [17] W. Yang, S. Lin, W. Gong, R. Lin, C. Jiang, X. Yang, Y. Hu, J. Wang, X. Xiao, K. Li, Y. Li, Q. Zhang, J. S. Ho, Y. Liu, C. Hou, H. Wang, *Science* 2024, 384, 74.
- [18] X. Yao, S. Zhang, N. Wei, L. Qian, S. Coseri, Adv. Fiber Mater. 2024, 6, 1256.
- [19] C. Ma, M. Wang, K. Wang, P. Uzabakiriho, X. Chen, G. Zhao, Adv. Fiber Mater. 2023, 5, 1392.

- [20] J. Huang, X. Yang, J. Yu, J. Han, C. Jia, M. Ding, J. Sun, X. Cao, Q. Sun, Z. L. Wang, Nano Energy 2020, 69, 104419.
- [21] H. Zhang, G. Li, H. Wei, X. Wu, S. Yan, Y. Xia, S. Yang, P. Schmuki, R. Cao, M. Zhu, Chem. Eng. J. 2024, 487, 150470.
- [22] J. Wang, B. Liu, D. Li, J. Yuan, D. Huang, C. Zhang, W. Song, C. Wang, J. Wang, L. Liu, Z. Han, L. Ren, Adv. Funct. Mater. 2025, 35, 2500701.
- [23] Z. Wu, J. Huang, Y. Zhao, X. Ding, J. Chen, Z. Liu, Z. Liu, Y. Zhu, Chem. Eng. J. 2025, 504, 158874.
- [24] Y. Wang, C. Sun, D. Ahmed, Nat. Electron. 2025, 8, 485.
- [25] K. Yoon, S. Lee, C. Kwon, C. Won, S. Cho, S. Lee, M. Lee, J. Lee, H. Lee, K.-I. Jang, B. Kim, T. Lee, Adv. Funct. Mater. 2025, 35, 2407759.
- [26] X. Yue, C. Fang, Q. Yao, C. Liu, C. Shen, H. Liu, Chem. Eng. J. 2024, 491, 151853.
- [27] R. Wang, T. Qiu, Y. Zhang, M. Rein, A. Stolyarov, J. Zhang, G. D. Seidel, B. N. Johnson, A. Wang, X. Jia, Adv. Funct. Mater. 2024, 34, 2403918.
- [28] Y. Lu, H. Zhang, Y. Zhao, H. Liu, Z. Nie, F. Xu, J. Zhu, W. Huang, Adv. Mater. 2024, 36, 2310613.
- [29] Y. Xu, S. Yu, L. Liu, W. Lin, Z. Cao, Y. Hu, J. Duan, Z. Huang, C. Wei, Z. Guo, T. Wu, Z. Chen, Q. Liao, Y. Zheng, X. Liao, Adv. Funct. Mater. 2024, 34, 2411331.
- [30] S. W. Cranford, A. Tarakanova, N. M. Pugno, M. J. Buehler, *Nature* 2012, 482, 72.
- [31] J. Wu, Z. Wu, Y. Wei, H. Ding, W. Huang, X. Gui, W. Shi, Y. Shen, K. Tao, X. Xie, ACS Appl. Mater. Interfaces 2020, 12, 19069.
- [32] Z. Wu, H. Ding, K. Tao, Y. Wei, X. Gui, W. Shi, X. Xie, J. Wu, ACS Appl. Mater. Interfaces 2021, 13, 21854.
- [33] D. Weng, F. Xu, X. Li, S. Li, Y. Li, J. Sun, ACS Appl. Mater. Interfaces 2020, 12, 57477.
- [34] Z. Wu, X. Yang, J. Wu, ACS Appl. Mater. Interfaces 2021, 13, 2128.
- [35] Q. Ding, Z. Wu, K. Tao, Y. Wei, W. Wang, B. Yang, X. Xie, J. Wu, Mater. Horiz. 2022, 9, 1356.